Spindle Dynamics Identification using Particle Swarm Optimization

Vasishta Ganguly and Tony L. Schmitz
Department of Mechanical Engineering and Engineering Science
University of North Carolina at Charlotte
Charlotte, NC, USA

ABSTRACT
Optimal parameters to eliminate machining chatter may be identified using analytical stability models which require the dynamics of the tool-holder-spindle-machine assembly. Receptance coupling substructure analysis (RCSA) provides a useful analytical tool to couple measured spindle-machine dynamics with tool-holder models to predict the tool point frequency response function for the assembly. Previous research has demonstrated a procedure to determine all required spindle receptances from a single measurement, where each mode within the measurement bandwidth was modeled as a fixed-free Euler Bernoulli beam and fit using a manual, iterative procedure. Here, a particle swarm optimization technique is described for fitting the spindle-machine measurement using a fixed-free Euler-Bernoulli beam model for each mode. The performance of the optimization process and RCSA in predicting the tool tip frequency response is evaluated and the results are presented.

KEYWORDS
Machining, Chatter, Receptance coupling substructure analysis, Particle swarm optimization.

INTRODUCTION

Machining instability (chatter) leads to poor surface finish, high rejection rates, rapid tool wear, and, potentially, spindle damage. Stable machining conditions may be identified using well-known milling process models [1-2]. This aids in pre-process parameter selection for optimal machining conditions. In order to identify stable machining conditions, the dynamics of the tool-holder-spindle-machine assembly as reflected at the tool tip is required. The frequency response function (FRF), which represents the structural dynamics, may be measured using modal techniques. In general, many different tool-holder combinations are used for a selected machining center. The cost of experimentally identifying the tool tip dynamics for each tool-holder combination may be prohibitively high in some cases. Receptance coupling substructure analysis (RCSA) provides a useful approach to predict the tool point response from a single measurement of the spindle-machine and models of the desired tool-holder combinations [3-8]. To complete the RCSA procedure, four spindle-machine receptances are required: displacement-to-force, displacement-to-couple, rotation-to-force, and rotation-to-couple. Only the former is convenient to measure. Therefore, in recent work [8], a procedure was described where each displacement-to-force mode in the measurement bandwidth was modeled as a fixed-free Euler-Bernoulli (EB) beam. Given an analytical description of each mode's fixed-free EB model, the other three receptances can be described analytically [3] for that mode and no additional measurements are required. The sum of the single mode fits are used to describe the four required spindle responses. This fitting procedure was manually completed mode-by-mode in the previous work. In this study, a particle swarm optimization (PSO) technique is implemented to automate the identification of the EB beam parameters for each mode.

The paper is structured as follows. First, a brief summary of RCSA and spindle dynamics identification is described. Second, a review of the PSO process is provided. Here, the PSO is specifically tailored to be robust enough to handle a variety of different FRFs. Third, experimental results from a vertical machining center are presented. Fourth, the performance of the PSO in identifying the spindle receptances and predicting the tool tip FRF is discussed. Finally, conclusions are presented.

RCSA BACKGROUND

RCSA enables assembly dynamics to be predicted when the receptances of the individual components are known. The receptances of the individual components may be modeled or measured. Conversely, the component receptances may be determined if the assembly receptances

(as well as the other component receptances) are known, again through either models or measurements. This is referred to as inverse RCSA. For milling applications, the tool-holder-spindle-machine may be separated into two individual components: (I) the tool (endmill) and holder combination; and (II) the spindle-machine. In practice, many different tool-holder combinations are used in machining operations. The tool-holder receptances may be modeled as free-free Timoshenko beams. On the other hand, it is challenging to model the spindle-machine receptances. Additionally, the spindle-machine receptances are subject to change over the lifetime of the spindle. Therefore, it is generally more convenient to experimentally identify the spindle-machine receptances and archive them for each machine. Once the spindle machine receptances are identified experimentally, they may be coupled with the tool-holder receptances using RCSA to predict the tool point direct FRF.

In order to experimentally identify the spindle-machine receptances, a standard artifact with the appropriate taper geometry (e.g., CAT or HSK) is inserted in the spindle. Figure 1 provides a schematic of the setup, where $\{U_i\} = \{X_i \ \Theta_i\}^T$ represents the assembly generalized displacement coordinates and consists of a displacement, X_i, and a rotation, Θ_i. $Q_i = \{F_i \ \ M_i\}^T$ represents the assembly generalized forces and consists of a force, F_i, and a couple (or moment), M_i. The four assembly receptances are then defined as:

$$G_{ij} = \begin{bmatrix} H_{ij} & L_{ij} \\ N_{ij} & P_{ij} \end{bmatrix}$$

where $\{U_i\} = [G_{ij}]\{Q_j\}$.

Similarly, $u_i = \{x_i \ \theta_i\}^T$ represents the component generalized displacement coordinates and consists of a displacement, x_i, and a rotation, θ_i. $q_i = \{f_i \ \ m_i\}^T$ represents the component generalized forces and consists of a force, f_i, and a couple (or moment), m_i. The component receptances are then defined as:

$$R_{ij} = \begin{bmatrix} h_{ij} & l_{ij} \\ n_{ij} & p_{ij} \end{bmatrix}$$

where $\{u_i\} = [R_{ij}]\{q_j\}$.

The direct, displacement-to-force FRF at the free end of the artifact-spindle-machine, H_{11}, assembly is measured. The direct, R_{11} and R_{2a2a}, and cross, R_{12a} and R_{2a1}, receptance matrices for the portion of the standard artifact beyond the flange are described using free-free Timoshenko beam models. The spindle-machine receptances at the flange, R_{2b2b}, are unknown. The assembly receptance at the tip can be defined as [4]:

$$G_{11} = R_{11} - R_{12a}(R_{2a2a} + R_{2b2b})^{-1}R_{2a1}, \qquad (1)$$

where R_{2b2b} is the only unknown. It is obtained by rearranging Eq. 1.

$$R_{2b2b} = R_{2a1}(R_{11} - G_{11})^{-1}R_{12a} - R_{2a2a} \qquad (2)$$

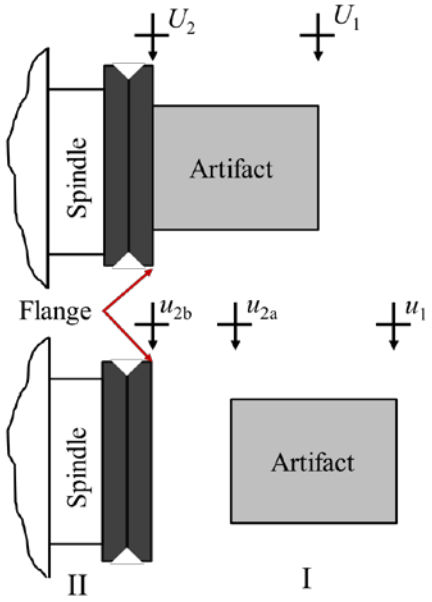

Figure 1. Schematic of the RCSA components.

As shown in Eq. 2, the receptances for the spindle-machine may be determined from the modeled direct and cross artifact receptances and the assembly receptances, G_{11}, where G_{11} consists of H_{11}, L_{11}, N_{11}, and P_{11} as previously described. $H_{11} = X_1/F_1$ can be measured using impact testing methods. Kumar and Schmitz [8] developed a method to fit the assembly response using multiple fixed-free EB beams. The number of EB beams corresponded to the number of modes within the measurement bandwidth. A manual, iterative approach was used to identify the individual beam geometries. Once the fixed-free EB beams were fit, the model parameters were used to compute L_{11}, N_{11}, and P_{11} [3] and fully populate the G_{11} matrix. The spindle-machine component receptances are then identified using Eq 2. These spindle receptances are coupled to modeled tool-holder receptances to predict the assembly tool point FRF.

Kumar and Schmitz [8] used the analytical, close-form EB beam receptances presented by Bishop and Johnson [3] to describe each measured displacement-to-force mode; see Eq. 3, where ω is the frequency (rad/s), d_j is the beam diameter, L_j is the beam length (m), ρ_j is the density (kg/m^3), E_j is the elastic modulus (N/m^2), η_j is the unitless solid damping factor, and f_{nj} is the natural frequency. The subscript j corresponds to the j^{th} mode.

$$H_{11}{}^{j} = \frac{\sin(\lambda_j L_j)\cosh(\lambda_j L_j) - \cos(\lambda_j L_j)\sinh(\lambda_j L_j)}{\lambda_j{}^{3} E_j I_j (1+i\eta_j)(\cos(\lambda_j L_j)\cosh(\lambda_j L_j) - 1)} \quad (3)$$

where

$$\lambda_j{}^{4} = \frac{\omega^2 \rho_j A_j}{E_j I_j (1+i\eta_j)}\ , A_j = \frac{\pi d_j{}^{2}}{4}\ , \text{and } I_j = \frac{\pi d_j{}^{4}}{64}.$$

For a given diameter, d_j, natural frequency, f_{nj}, density, ρ_j, and elastic modulus, E_j, the beam free length is obtained from a closed form expression for the natural frequency of a fixed-free cylindrical beam [9]; see Eq. 4. This free length of the beam is used in Eq. 3.

$$L_j = \left(\frac{1.87510407^2 d_j}{2\pi f_{n_j}} \left(\frac{E_j}{16\rho_j} \right)^{\frac{1}{2}} \right)^{\frac{1}{2}} \quad (4)$$

All the beams were modeled assuming the material properties of steel (ρ = 7800 kg/m^3 and E = 200 GPa). Then, for each mode within the measured bandwidth, a corresponding diameter, d_j, solid damping factor, η_j, and a natural frequency, f_{nj}, was identified by an iterative process such that the combined receptance for all modes accurately represents the fit displacement-to-force receptance, $H_{11}{}^{f}$; see Eq. 5.

$$H_{11}{}^{f} = \sum_{j=1}^{no.\ of\ modes} H_{11}{}^{j} \quad (5)$$

In this study a particle swarm optimization technique is applied to identify the fixed-free EB beam properties. This considerably reduces the time to identify the beam parameters relative to the manual, iterative fitting procedure. The optimization objective is to minimize the difference between the fit receptance and the measured receptance, $H_{11}{}^{m}$. For each mode within the measured bandwidth, a fixed-free beam is identified with an optimal beam diameter, d_j, natural frequency, f_{nj}, and solid damping ratio, η_j, in order to minimize the error between $H_{11}{}^{f}$ and $H_{11}{}^{m}$. The objective function, O, was defined as:

$$O = \sqrt[2]{\begin{matrix} \left\{ Re(H_{11}{}^{m}) - Re(H_{11}{}^{f}) \right\}^2 \\ + \left\{ Im(H_{11}{}^{m}) - Im(H_{11}{}^{f}) \right\}^2 \end{matrix}} \quad (6)$$

where *Re* indicates the real part and *Im* indicates the imaginary part of the fit and measured receptances.

The total number of variables for the optimization problem is three times the total number of modes identified within the measured bandwidth because there are three beam parameters (diameter, solid damping factor, and natural frequency) to be identified for each mode. Once the equivalent beam geometries have been identified using the optimization process, the other receptances of the G_{11} matrix are identified using Eqs. 7-9.

$$L_{11}{}^{j} = N_{11}{}^{j} = \frac{-\sin(\lambda_j L_j)\sinh(\lambda_j L_j)}{\lambda_j{}^{2} E_j I_j (1+i\eta_j)(\cos(\lambda_j L_j)\cosh(\lambda_j L_j) - 1)} \quad (7)$$

$$P_{11}{}^{j} = \frac{\sin(\lambda_j L_j)\cosh(\lambda_j L_j) + \cos(\lambda_j L_j)\sinh(\lambda_j L_j)}{\lambda_j E_j I_j (1+i\eta_j)(\cos(\lambda_j L_j)\cosh(\lambda_j L_j) - 1)} \quad (8)$$

$$[L/N/P_{11}]^{f} = \sum_{j=1}^{no.\ of\ modes} [L/N/P_{11}]^{j} \quad (9)$$

PARTICLE SWARM OPTIMIZATION PROCESS

The particle swarm optimization (PSO) algorithm is a population-based optimization algorithm which may be used to address a variety of engineering problems. The PSO technique, proposed by Kennedy and Eberhart [10], was motivated by the need to develop models for social behavioral simulations, such as the movements of a flock of birds or a school of fish. It has since been applied directly to optimization problems. The population is referred to as a swarm and each individual within the population is a particle.

Computationally, each particle within the swarm represents a vector. The vector is composed of the variables which constitute the optimization problem. The number of variables within the vector corresponds to the number of variables which must be optimized. These variables represent the position of the particle within the feasible design space. A fitness, or objective, function is constructed to represent the optimization problem.

The objective function is typically a minimization function which represents the error between some measured value and a corresponding simulated value. The simulated value is obtained from a model using the variables which constitute the optimization problem; see Eq. 6. Once a fitness value is evaluated for each particle within the swarm, the particle closest to the best solution may be identified, that is, the particle with the best fitness value. Knowledge of the position of the particle with the best fitness value, as well as the position of each particle within the swarm, can be used to direct each particle towards the region in the solution space with the optimal solution. At each step of the optimization process the particle with the best fitness value is identified and, based on its position in the design space, a velocity vector is generated. The position of each particle is then updated to move towards the optimal solution. The velocity vector does not depend only on the position of the best particle. The algorithm maintains a record of the best position of each individual particle as its position within the design space is updated at each iteration of the optimization process. A component of the velocity vector for each individual particle also depends on its own previous best position. The component of the velocity vector which depends on the global best position among all the particles in the swarm may be thought of as “publicized knowledge”, while the component which depends on each particles own personal best position may be thought of as “simple nostalgia” [10]. An additional

inertia term which depends on the velocity in the previous optimization step is also occasionally included. The velocity vector and the updated position of the particle are obtained from Eqs. 10-11:

$$V_i = wV_{i-1} + C_pR_p(X_p - X_i) + C_gR_g(X_g - X_i) \quad (10)$$

$$X_i = X_{i-1} + V_i \quad (11)$$

where

X_i : position of particle at the i^{th} iteration
X_{i-1} : position of particle at the $(i\text{-}1)^{th}$ iteration
V_i : velocity of particle at the i^{th} iteration
V_{i-1} : velocity of particle at the $(i\text{-}1)^{th}$ iteration
w : inertia weight
X_p : position of personal best
X_g : position of global best
C_p : personal weight
R_p : random number between zero and one
C_g : global weight
R_g : random number between zero and one.

The inertia weight controls the contribution of the velocity of the particle in the previous step. A large inertia weight facilitates a broader exploration of the design space and gives the algorithm its global nature [11]. This aids in avoiding local minima. The inertia weight is often updated at each optimization step and is gradually reduced to zero. The personal weight also facilitates the design space exploration. A high value of the global weight facilitates the rapid exploitation of the knowledge of the position of the best particle within swarm. The random numbers, R_p and R_g, are required to introduce "craziness" to the optimization process, which is required to avoid local minima [10]. In all evolutionary (e.g., genetic) or population-based (e.g., PSO) optimization algorithms, an agreeable balance between exploratory and exploitatory behavior is necessary in order to adequately search the design space and avoid local minima, while simultaneously ensuring convergence on the best solution. In this study, the inertia weight was found to be unnecessary and the equation for velocity was truncated to eliminate the inertia component. The larger the number of particles in the swarm, the greater the extent of the design space initially explored.

Typically, the variables in any optimization problem have lower and/or upper limits of acceptable values. These bounds define the feasible design space. While updating the position of some particles during the optimization process, they may fall outside the feasible design space. In this case, the position of the particle is not updated and the particle retains the same position as in the previous optimization step.

In the following sections the different steps in the optimization process tailored to identify the equivalent fixed-free EB beam parameters are discussed. Measurements on a Haas TM-1 CNC machining center are used to illustrate the optimization process. Further details of the measurement parameters are provided in the next section. The authors recognize that other optimization algorithms may also be suitably tailored to solve the same optimization problem.

Step 1: Individual mode identification

In this step, the different modes within the measured bandwidth are identified. For tool point direct FRFs ($H_{11}{}^m$), the imaginary part of the response is purely negative. Therefore, the natural frequencies of the different modes may be identified by searching for negative peaks in the imaginary part of the FRF. The mode identification algorithm compares each element within a vector with its neighboring elements and recognizes those which are less than both its neighboring elements, i.e., the search is for negative peaks. This method is highly susceptible to noisy response data. This was addressed by incorporating a moving average filter which serves to smooth the (potentially) noisy data. The number of points which defines the moving average filter is defined as the horizontal sensitivity factor, H_{sens}. This value is defined by the optimizer through visual inspection of the real and imaginary parts of response function. A low H_{sens} value retains noise susceptibility, while a high value may miss closely-spaced modes along the frequency axis. A vertical sensitivity factor, V_{sens}, is also defined, which establishes a cutoff limit as a percentage of the magnitude of the imaginary part of the most flexible mode. All the modes with an imaginary part amplitude less than the cutoff limit (i.e., very stiff modes) are ignored. Figure 2 shows the real and imaginary parts of a measured FRF (experimental setup details provide in a later section). The selected peaks are identified by crosses. The effect of H_{sens} is demonstrated in Figure 3. The figure shows a magnified portion of the response. When H_{sens} = 1, three modes (circles) are identified in this region, but when H_{sens} = 21, only one mode (cross) is recognized. The difference in the FRFs plotted in Figure 3 is due to the effect of the moving average filter. It should be noted here that, although the natural frequencies for the modes were identified in this step itself, they remained as variables in the optimization process. This was not completely necessary, but it did provide some flexibility to account for any errors in the selected frequencies.

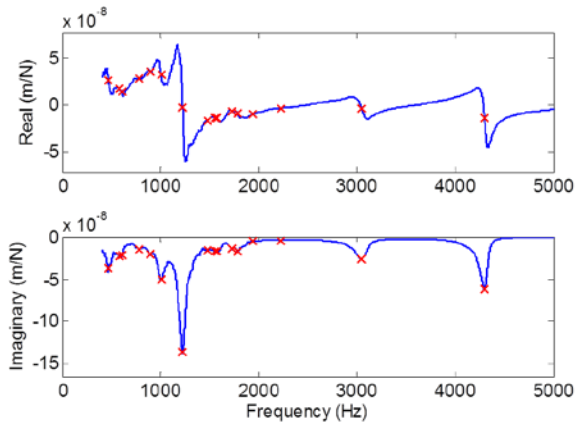

Figure 2. Measured direct frequency response function (H_{11}^{m}) with selected modes (crosses).

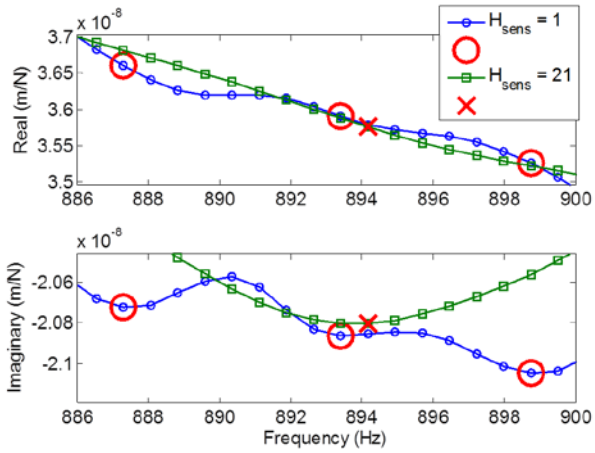

Figure 3. The effect of H_{sens} on peak identification (H_{sens} = 1: circles; H_{sens} = 21: cross).

Step 2: Generating optimization points

The FRF data is measured at equally spaced increments along the frequency axis. The resolution of the points along the frequency axis depends on the sampling rate and number of data points. A large number of the data points naturally exist at frequencies where there is no mode. These points provide little valuable information to the optimization process. Therefore, an attempt was made to concentrate more data points near the mode peaks. To reduce the total number of points, the distribution of points along the frequency axis was made proportional to the magnitude of the FRF. This ensured more data points at regions of high magnitude which are typically near the modes. This was achieved by using the *randsample* command in Matlab®. The magnitude of the frequency response function was used as the weighting function to distribute points along the frequency axis. Figure 4 shows a plot of the individual points overlaid on the magnitude plot of the frequency response functions as well as the histogram of the point distribution along the frequency axis. As seen in the Figure 4 histogram, there is a concentration of points at locations where the frequency response function has the highest magnitude (at the modes). Figure 5 shows the point distribution between 3000 Hz and 4400 Hz. It is clear that there is a higher concentration of points near the mode peaks. Once these points have been generated, the real and imaginary parts of the response are evaluated at these newly generated points along the frequency axis using interpolation. This greatly reduced the computational time.

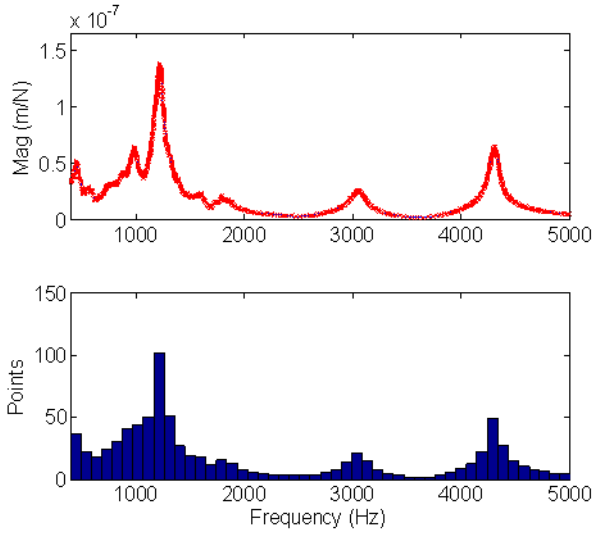

Figure 4. Histogram of points showing concentration of points at nodes.

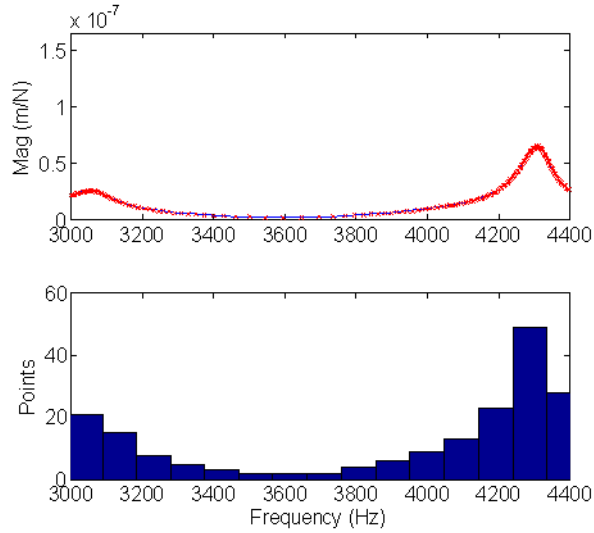

Figure 5. Histogram of points between 3000 Hz and 4400 Hz showing fewer points away from the modes.

Step 3: Optimization for each individual mode

Before optimizing for the combined response of all the modes together, PSO subroutines were executed over small frequency ranges to identify the diameter, solid damping factor, and natural frequency for each mode independently. These parameters were used to specify the lower and upper bounds of the design space when optimizing for the combined response of all the fixed-free EB beams together. This ensured faster convergence towards the optimal solution when optimizing for the combined FRF. The equation for $H_{11}{}^{f}$ (Eq. 6) was modified to include only the mode under consideration. When optimizing for the individual modes, the objective function was also modified to include only the imaginary part of the FRF. The real part of the measured FRF in the frequency region of the mode under consideration is typically offset along the vertical axis due to effects of neighboring modes.

When optimizing for the individual modes, only the data points of the FRF within a frequency range around the mode under consideration were considered. However, caution was exercised when defining this frequency range. If the range was too small, there was not sufficient response data to find an optimal solution which accurately represented the contribution of the mode under consideration to the combined response. If the selected was too large, the response data could be polluted by contributions of the neighboring modes, resulting in errors in the optimal beam parameter predictions for the mode under consideration.

A number of different constraints were established to identify the optimization frequency range for the individual modes. The lower and upper limits for the frequency range for the j^{th} mode were defined as $\delta f^{j}{}_{lower}$ and $\delta f^{j}{}_{upper}$, respectively. The natural frequency of the j^{th} mode identified in step one was defined as f_m^j. The constraints are then described as:

a) $\delta f^{j}{}_{lower} < 0.5(f_m^{j-1} - f_m^j) - 5 \quad f_m^0 = 0$
$\delta f^{j}{}_{upper} < 0.5(f_m^j - f_m^{j+1}) - 5 \quad f_m^{no.\ of\ modes\ +1} = 10$ kHz

b) $\delta f^{j}{}_{lower} < 200$ Hz
$\delta f^{j}{}_{upper} < 200$ Hz

c) $\delta f^{j}{}_{lower} / \delta f^{j}{}_{upper} < 5$
$\delta f^{j}{}_{upper} / \delta f^{j}{}_{lower} < 5$

Constraint a) ensured that $\delta f^{j}{}_{lower}$ and $\delta f^{j}{}_{upper}$ were not greater than half the distance to the adjacent mode, but instead fall short by at least 5 Hz. Constraint b) ensured that $\delta f^{j}{}_{lower}$ and $\delta f^{j}{}_{upper}$ were not greater than 200 Hz from the natural frequency of the mode under consideration. Constraint c) ensured that the ratio of $\delta f^{j}{}_{lower}$ to $\delta f^{j}{}_{upper}$ was no more than five. The inverse was also held true. This ensured that the frequency range for optimization for a single mode was not unevenly distributed about the natural frequency for that mode. These constraints were developed on a trial and error basis, with continuous verification to ensure that they were robust for different frequency response functions. Once the frequency range for optimization for each individual mode was identified, optimization for the equivalent fixed-free EB beam parameters was carried out as previously described. The mode near 1220 Hz is used to demonstrate the process.

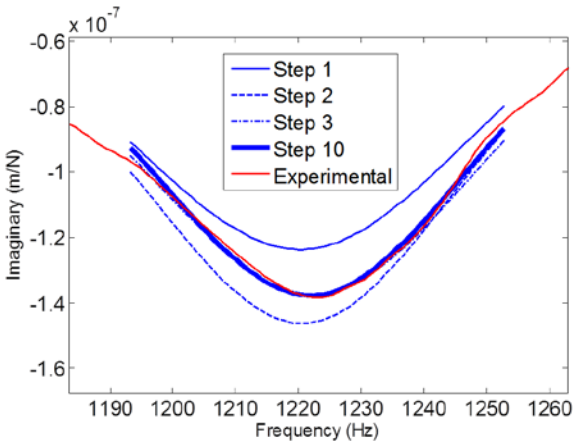

Figure 6. Optimal fit at different steps of the individual mode optimization process for mode at 1220 Hz.

Figure 6 shows the imaginary part of the measured response as well as of the simulated optimal solution at different iterations (steps 1, 2, 3, and 10) of the optimization process. As seen from the figure, the algorithm rapidly converges to the measurement. The position of the particles in the swarm along with their fitness values (gray-scale color bar) at the different optimization steps are plotted in Figure 7. The particles in the swarm in the first optimization step are randomly positioned, but they rapidly converge on the best solution.

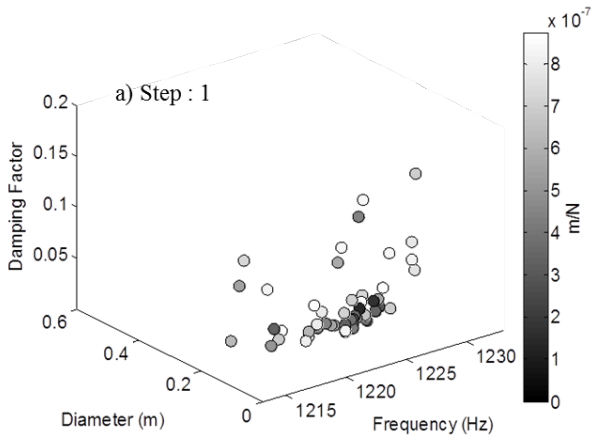

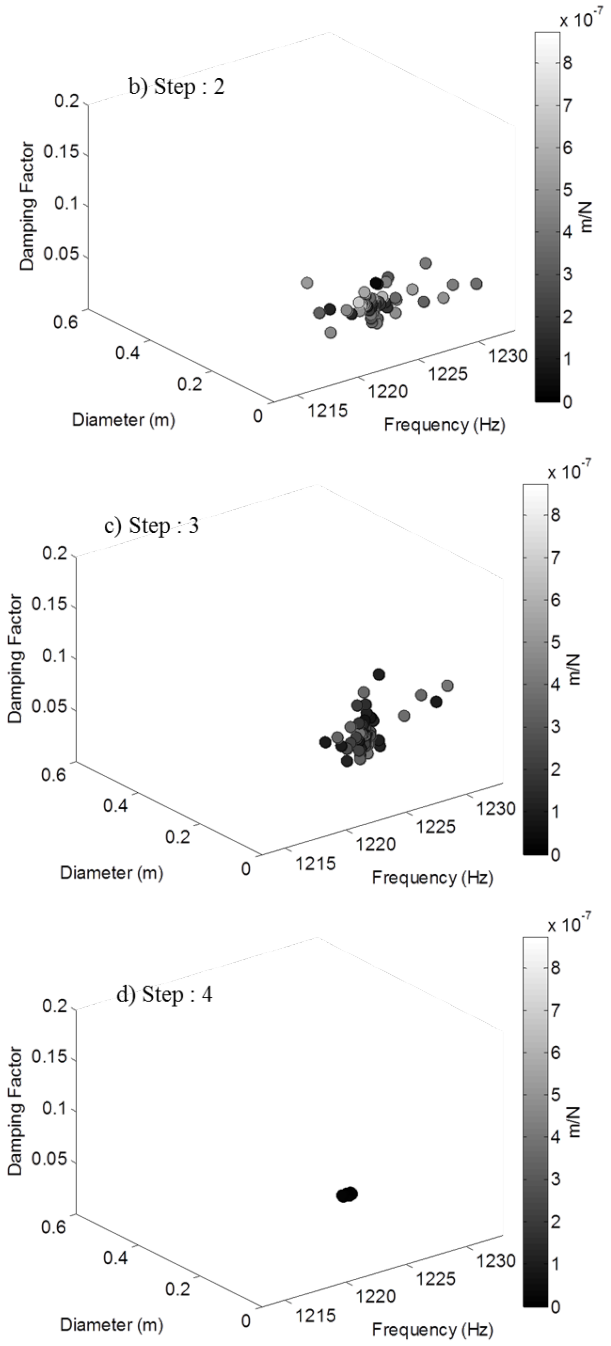

Figure 7. Position of particles in the swarm at optimization steps: a) 1; b) 2; c) 3; and d) 10.

Step 4: Optimization for all modes

Once the diameter, solid damping factor, and natural frequency are identified for all the different modes as described in step three, these optimized values were used to set the limits of the design space when optimizing for the combined effects for all modes simultaneously. For the diameter and solid damping factors, the lower bounds were set at 50% the optimal values and the upper bounds were set at 150% the optimal values. The natural frequency for each mode was allowed to vary within an 80 Hz range centered about the optimal natural frequency for that mode.

EXPERIMENTAL RESULTS

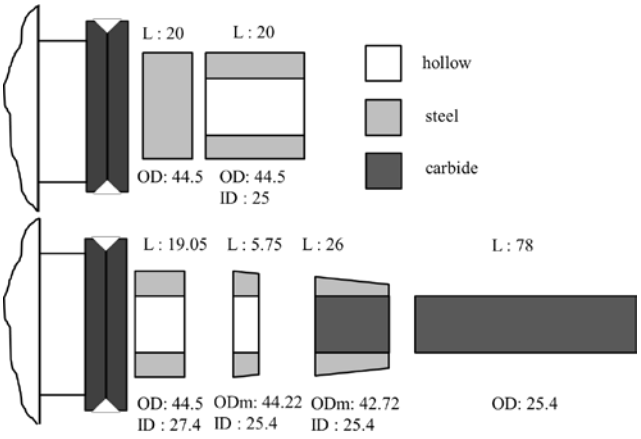

Figure 8. Schematic illustration of the spindle artifact and tool-holder assembly. All dimensions are in mm.

Experiments were conducted on a Haas TM-1 CNC machining center. The dimensions of the artifact and tool-holder combination are provided in Figure 8. A 25.4 mm diameter solid carbide blank was used as the tool. A thermal shrink fit (Shrinker) tool holder was used to mount the carbide tool in the machine spindle (CAT-40 taper). Both the artifact and the tool holder-tool combination were modeled as constant cross-section slices. The assembly receptances were obtained by coupling the free-free boundary condition slices using RCSA.

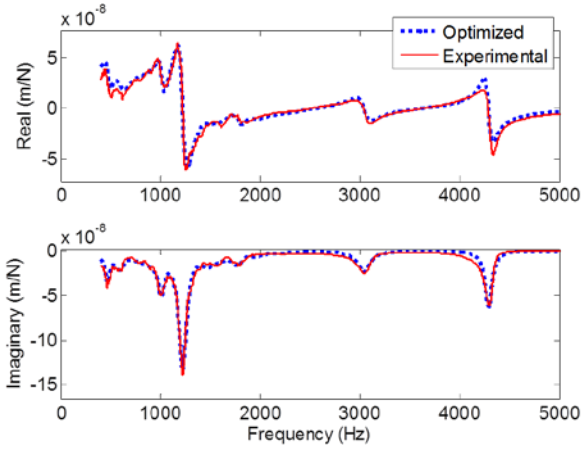

Figure 9. Comparison of fit and measured H_{11} direct FRF measured at the free end of the spindle artifact.

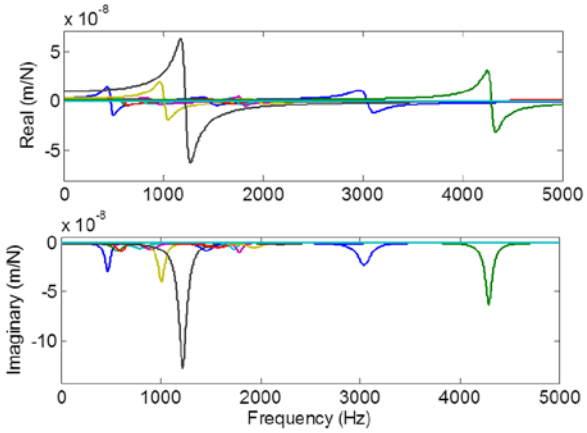

Figure 10. Individual $H_{11}{}^{f}$ FRFs for the individual fixed-free EB beams.

Figure 9 shows the comparison of the measured FRF at the free end of the artifact mounted in the machined spindle and the optimal FRF obtained by fitting the equivalent fixed-free EB beams. Good agreement was found between the experimental and optimized FRFs. Figure 10 shows the real and imaginary parts of the individual FRFs for each of the optimized modes. The assembly FRF was obtained by summing all the individual FRFs; see Eq. 5. The optimal values for the equivalent fixed-free EB beam diameter, solid damping factor, and natural frequency are listed in Table 1. The corresponding beam lengths (Eq. 4) are also listed. The PSO process parameters are listed in Table 2.

Table 1. Optimal fixed-free EB beam parameters.

Mode #	Natural frequency Hz	Diameter m	Solid damping factor -	Length m
1	468	0.196	0.122	0.545
2	575	0.231	0.212	0.533
3	602	0.255	0.144	0.547
4	795	0.213	0.239	0.435
5	904	0.209	0.172	0.405
6	1007	0.132	0.078	0.305
7	1220	0.073	0.079	0.206
8	1465	0.181	0.098	0.295
9	1551	0.173	0.185	0.281
10	1576	0.172	0.178	0.278
11	1737	0.237	0.045	0.311
12	1789	0.227	0.034	0.300
13	1941	0.191	0.096	0.264
14	2205	0.226	0.153	0.269
15	3040	0.102	0.048	0.154
16	4289	0.080	0.020	0.115
17	5994	0.102	0.035	0.110
18	8630	0.1363	0.044	0.106

Table 2. PSO optimization parameters.

Description	Value
H_{sens}	21
V_{sens}	3%
Individual mode optimization subroutine	
Swarm size	200
Maximum iterations	20
C_q	2
C_p	3
Optimization for all modes	
Swarm size	100
Maximum iterations	100
C_q	2
C_p	4

Once the equivalent fixed-free EB beam parameters were identified, the other receptances, L_{11}, N_{11}, and P_{11}, were calculated using Eqs. 7-9. Combined, these receptances completely populate the G_{11} matrix. Figure 11 (top) shows L_{11} and N_{11}. Note that they are identical; see Eq. 7. The P_{11} receptance is displayed in Figure 11 (bottom).

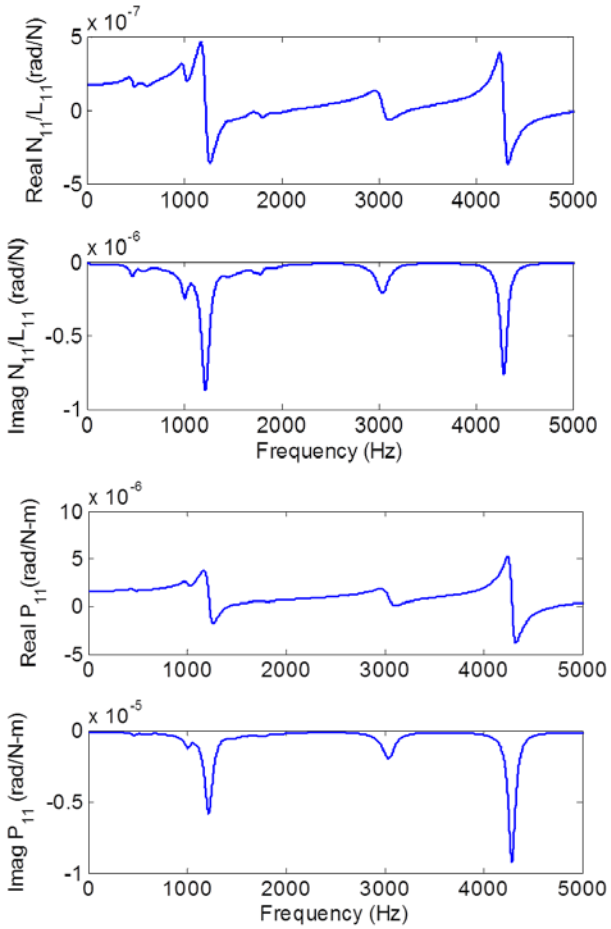

Figure 11. Simulated L_{11} and N_{11} (top) and P_{11} (bottom) receptances at the free end of the artifact.

The spindle receptances, R_{2b2b}, were computed by decoupling the modeled artifact receptances (for the portion of the artifact beyond the flange) using Eq. 2. The artifact was modeled as a free-free Timoshenko beam. Figure 12 shows the h_{2b2b} (top), $l_{2b2b} = n_{2b2b}$ (middle), and p_{2b2b} (bottom) receptances that populate the R_{2b2b} matrix.

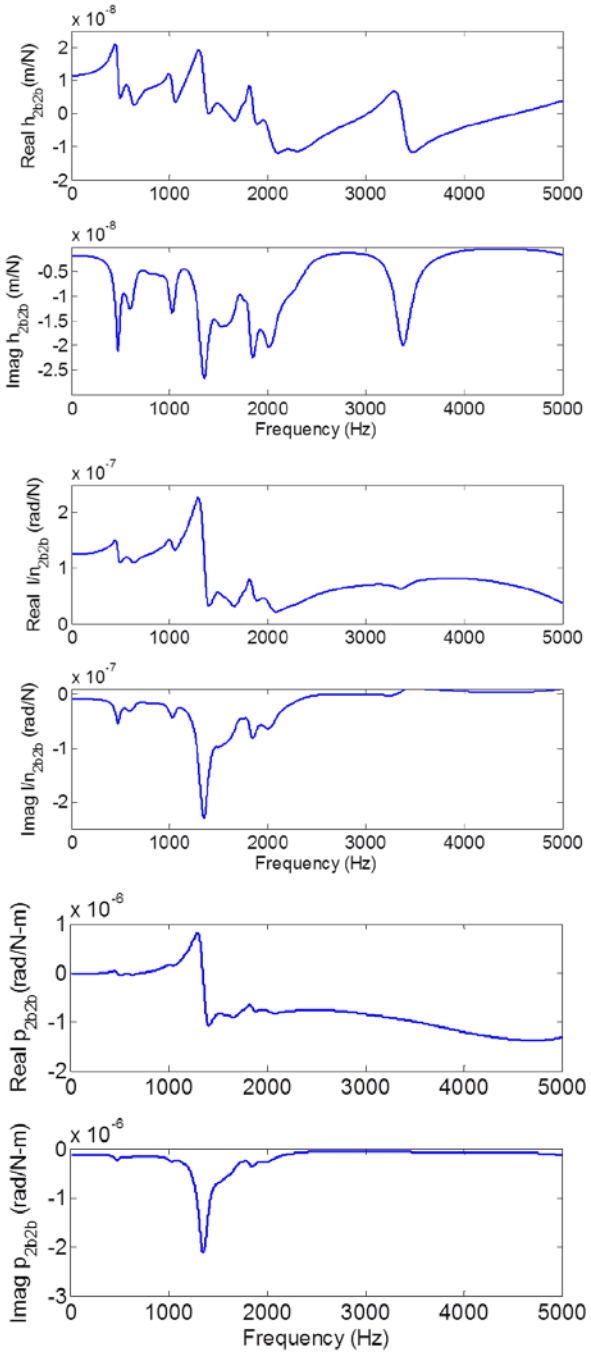

Figure 12. Spindle receptances: h_{2b2b} (top), $l_{2b2b} = n_{2b2b}$ (middle), and p_{2b2b} (bottom).

The spindle receptances are then coupled with modeled receptances for the tool-holder using Eq. 1 to predict the tool tip FRF. In this case, the R_{11} and R_{2a2a} direct receptances and the R_{12a} and R_{2a1} cross receptances are computed for the tool-holder. The assembly tool tip FRF is shown in Figure 13. The measured tool tip FRF is also shown. It is seen that the simulated FRF natural frequencies match well with the measured FRF natural frequencies. However, the magnitude of the simulated FRF was found to be less than the measured FRF magnitude for the 850 Hz mode. There are a high number of modes within the first 2000 Hz of the h_{2b2b} spindle-machine receptances; see Figure 12 (top). These modes interact with the first bending mode of the tool holder-tool assembly when coupled. Small errors in the fit/calculated spindle-machine responses therefore lead to errors in the magnitude predictions for the tool-holder-spindle-machine assembly FRF.

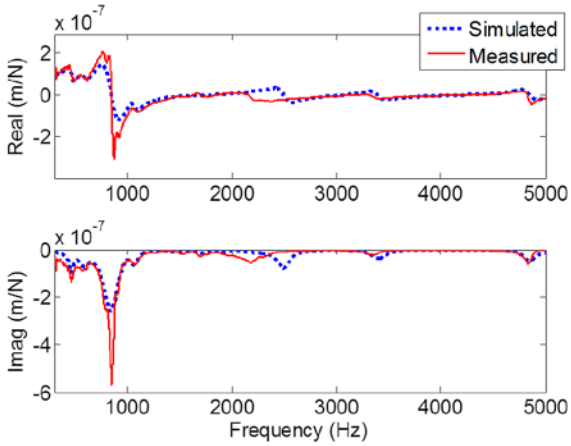

Figure 13. Predicted(dotted line) and measured (solid line) H_{11} receptances for the tool-holder-spindle-machine.

CONCLUSIONS

It was shown that receptance coupling substructure analysis (RCSA) provides a useful tool to couple and decouple structural elements in order to identify the frequency responses for both assembly and components. This is particularly useful in machining dynamics analysis. The frequency response of the spindle-machine is identified experimentally and archived. The spindle-machine receptances are then coupled to modeled receptances for any selected tool-holder combination to predict the tool tip frequency response. In previous work, Kumar and Schmitz used fixed-free EB beams to represent each mode in the spindle-machine displacement-to-force measurement [8]. Using the beam parameters estimated from a manual, iterative process, the required displacement-to-couple, rotation-to-force, and rotation-to-couple receptances can be calculated.

In this study, fitting process was automated using a particle swarm optimization technique. The optimization method was shown to successfully identify beam parameters which produced a FRF that matched well with the measured frequency response. The tool tip FRF predicted using RCSA was also found to agree with the measured FRF, particularly in frequency.

REFERENCES

[1] Smith, S. and Tlusty, J., 1991. An overview of modeling and simulation of the milling process. Journal of Engineering for Industry, 113/2: 169-175.

[2] Altintas, Y. and Weck, M., 2004. Chatter stability of metal cutting and grinding. Annals of the CIRP, 53/2: 619-642.

[3] Bishop, R.E.D., Johnson, D.C., 1960. The Mechanics of Vibration. Cambridge University Press, Cambridge, UK.

[4] Schmitz, T., Smith, K. S., 2009. Machining Dynamics: Frequency Response to Improved Productivity. Springer, New York, NY.

[5] Schmitz, T., Donaldson, R., 2000. Predicting high-speed machining dynamics by substructure analysis. Annals of the CIRP, 49/1: 303-308.

[6] Schmitz, T., Davies, M., and Kennedy, M., 2001. Tool point frequency response prediction for high-speed machining by RCSA. Journal of Manufacturing Science and Engineering, 123: 700-707.

[7] Schmitz, T., Duncan, G.S., 2005. Three-component receptance coupling substructure analysis for tool point dynamics prediction. Journal of Manufacturing Science and Engineering, 127/4: 781-790.

[8] Kumar, U. V., Schmitz, T.L., 2012. Spindle dynamics identification for Receptance Coupling Substructure Analysis. Precision Engineering, 36: 435-443.

[9] Blevins, R., 2001. Formulas for Natural Frequency and Mode Shape. Krieger Publishing Co., Malabar, FL.

[10] Kennedy, J., Eberhart, R. C., 1998. Particle swarm optimization. Proceeding of the IEEE International Conference on Evolutionary Computation, Piscataway, NJ. IEEE Press 1998: 69-73.

[11] Shi, Y., Eberhart, R.C., 1999. Empirical study of particle swarm optimization. Proceeding of the 1999 Congress on Evolutionary Computation. CEC 1999, 3: 1945-1950.